Chapter 7
Opacity and Radiation Transport

Abstract When an intense laser is irradiated on medium and high Z materials, large amount of energy is converted to x-rays and transported as radiation in plasmas. The same kind of transport equation as the electrons should be solved for the radiation energy spectrum. The tuff issue for the case of non-local electron transport modeling was the inclusion of the effect of electric and magnetic fields. Instead, the photons can be assumed to travel with straight path, while the problem is physical modeling of opacity, especially when the plasma is partially ionized and line radiation transport is important. So, the modeling of spectral opacity and emissivity of partially ionized plasma becomes challenging. It has been studied for a long time in astrophysics regarding the evolution of stars etc. More challenging point in laser plasma is caused by the fact that the plasma is small but high-density, so that the laser plasma is optically thick in some case. With intense lasers, spectral opacity has been studied experimentally and opacity codes have been improved. Finally, neutrino transport in gravitationally-collapsing supernovae is also explained as a topic that the hydrodynamic instability is strongly affected by local and non-local transport by neutrino.

7.1 Radiation Transport

When an intense laser is irradiated on medium or high Z solid targets, substantial amount of absorbed plasma energy is converted to the energy of radiation. In general, the energy rage of such photons is up keV, since the plasma temperature becomes from eV to keV. The fraction of radiation increases as the increase of Z-number of the target material. Even for plastic targets, about 10% of the absorbed energy escaped from the plasma into vacuum as radiation. So, modeling radiation emission, absorption, and transport in laser plasma is very important for time evolution of hydrodynamics.

Let us see how radiation is important in laser-produced plasma. The bremsstrahlung emission from free electrons with ionization degree Z is given in (5.163). Evaluate the cooling time [s] of the plasma roughly as follows.

H. Takabe, *The Physics of Laser Plasmas and Applications - Volume 2*,
Springer Series in Plasma Science and Technology,
https://doi.org/10.1007/978-3-031-45473-8_7

$$\frac{1}{\tau_c} \sim \frac{J}{n_e T_e} \sim 10^{-7} Z^2 n_i \frac{1}{\sqrt{T_{eV}}} \tag{7.1}$$

where the ion density n_i in cm^{-3} and electron temperature T_{eV} in eV unit. Inserting a typical values of laser plasma and targets, the local radiation cooling time by Bremsstrahlung emission is given as

$$\tau_c \sim 10^{-12} \frac{1}{Z^2} \left(\frac{n_i}{10^{20} cm^{-3}} \right)^{-1} \sqrt{\frac{T_e}{100eV}} \quad [s] \tag{7.2}$$

This is very short time scale compared to that of hydrodynamics for laser produced plasma and indicates that the radiation transport should be modeled in hydrodynamic codes to evaluate the radiation cooling and heating in (2.108). In addition, radiation absorption and transport are found to be important in analyzing laser produce plasma dynamics.

Note that (7.1) is the cooling time of plasma due to Coulomb interaction of electrons with ions for the case where there is no absorption of radiation in the plasma. It is clear that even hydrogen plasma the cooling time is very short compared to the laser pulse of ns if a solid hydrogen is heated by laser. It is, then, important to solve radiation transport equation in plasma with appropriate opacity and emissivity as a function of radiation frequency. The opacity and emissivity by free electrons are already given in Chap. 5.10. We have to model the opacity and emissivity due to electron transition between bound states and bound and free states. For this purpose, atomic model is required as described in Chap. 5.

Let us consider a modeling of radiation transport with assumption that the spectral opacity and emissivity are given. The basic equation for the radiation transport is almost the same as Fokker-Planck equation except for several difference. It is given as a kinetic equation for radiation energy flux vector I^{ν} of frequency ν.

$$\frac{1}{c} \frac{\partial}{\partial t} I^{\nu}(t, \boldsymbol{r}, \boldsymbol{\Omega}) + \boldsymbol{\Omega} \cdot \nabla I^{\nu}(t, \boldsymbol{r}, \boldsymbol{\Omega}) = \eta^{\nu}(t, \boldsymbol{r}) - \chi^{\nu}(t, \boldsymbol{r}) I^{\nu}(t, \boldsymbol{r}, \boldsymbol{\Omega}) \tag{7.3}$$

In (7.3), $\boldsymbol{\Omega}$ is a direction of radiation propagation, and η^{ν} and χ^{ν} are spectral emissivity and opacity, respectively. In (7.3), it is also assumed that the photons propagate straight with the speed of light c and the effect of refraction is neglected, because the photon energy carrying most of energy is in the rage of 100 eV and the cut-off frequency of the photon is higher than the maximum electron density.

Note that it is very hard to solve (7.3) directly, because I^{ν} is a function of t, $\mathbf{r}$, and $\boldsymbol{\Omega}$, totally 6 dimensions. In addition, multi-group transport for photon energy should be solved. In what follows, consider the case of one-dimension in real space. And, let us assume that the photon angle distribution along the direction of non-uniformity is only a function of θ same as in Fig. 6.2. Then, in case of plane geometry (7.3) reduces to

$$\frac{1}{c}\frac{\partial}{\partial t}I^{\nu}+\mu\frac{\partial}{\partial x}I^{\nu}=\eta^{\nu}-\chi^{\nu}I^{\nu} \tag{7.4}$$

It is as follows in spherically symmetric geometry.

$$\frac{1}{c}\frac{\partial}{\partial t}I^{\nu}+\mu\frac{\partial}{\partial r}I^{\nu}+\frac{(1-\mu^2)}{r}\frac{\partial}{\partial \mu}I^{\nu}=\eta^{\nu}-\chi^{\nu}I^{\nu} \tag{7.5}$$

Let us assume that the radiation field is always in steady state for time-varying opacity and emissivity and time derivatives in (7.4) and (7.5) can be neglected. With a typical size of the laser plasma as L, the transit time of photons in plasma is $\Delta t = L/c$ and it is about 3 ps for $L = 100$ μm. It is a good approximation to neglect this time scale in the plasma produced by ns pulse lasers. Then, (7.4) is rewritten in the form.

$$\frac{d}{d\tau_{\nu}}I^{\nu}+I^{\nu}=S^{\nu} \tag{7.6}$$

where τ_{ν} is **optical depth** and defined as

$$d\tau_{\nu}=\frac{\chi^{\nu}}{\mu}dx=\chi^{\nu}dl \tag{7.7}$$

where dl is a path length of photon propagation. In (7.6), Sn is called **source function** defined as

$$S^{\nu}=\eta^{\nu}/\chi^{\nu} \tag{7.8}$$

It should be noted that the source function is Planck distribution if the plasma matter is in LTE condition, because I^{ν} in (7.3) should be Planck distribution at steady state and in uniform matter in LTE. In laser plasma, however, atomic state is not in LTE in general as discussed in Chap. 5.

It is easy to integrate (7.7) to obtain the solution for the case with a plane geometry with a finite plasma from x = 0 to x = d.

$$\begin{aligned} I^{\nu}(x) &= e^{-\tau_{\nu}(x)}\left(I^{\nu}_{(0,\mu)}+\int_0^x e^{\tau_{\nu}}S^{\nu}_{(x)}d\tau_{\nu}\right) \quad \text{for } \mu>0 \\ &= e^{-\tau'_{\nu}(x)}\left(I^{\nu}_{(d,\mu)}+\int_x^d e^{\tau'_{\nu}}S^{\nu}_{(x)}d\tau'_{\nu}\right) \quad \text{for } \mu<0 \end{aligned} \tag{7.9}$$

where τ_{ν} and τ'_{ν} are optical depths integrated as follows.

$$\tau_\nu = \frac{1}{\mu}\int_0^x \chi^\nu dx, \qquad \tau'_\nu = \frac{1}{|\mu|}\int_x^d \chi^\nu dx \tag{7.10}$$

It is straightforward to extend the above calculation in solving the case of spherical geometry (7.5). Introducing the impact parameter "b" like Coulomb collision in spherical potential, it is easy to formulate the solution.

It is useful to show the angle distribution of radiation flux for the case when an intense laser is irradiated on a gold foil [1]. Based on average ion model to be shown in Chap. 8 spectral emissivity and opacity of gold plasma is calculated with collisional radiative equilibrium assumption for 100 energy group up to 3 keV. The plane target is divided to 120 groups. In Fig. 7.1, a typical angular distribution of spectral integrated radiation flux is shown for four different target positions with normalized intensity at each position. The positions are shown with Lagrangian mesh points. The point i = 120 is the ablating plasma front. Since the optical depth is large in (7.10) for oblique direction $\mu \to 0$, the radiation flux is larger.

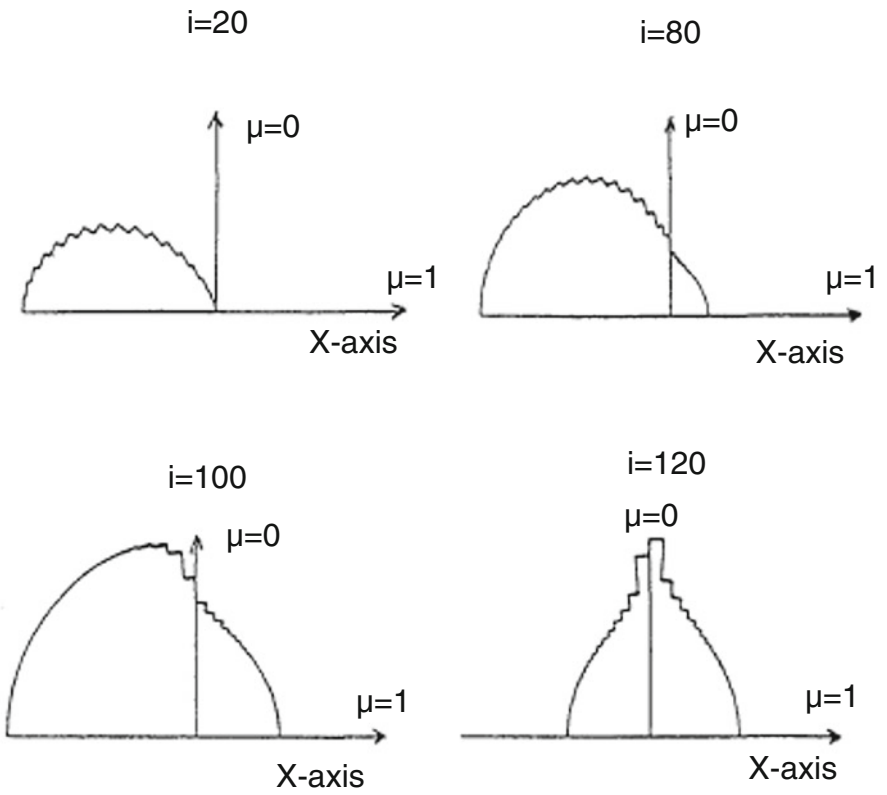

Fig. 7.1 Angular distribution of radiation intensity in gold plasma produced by irradiation of intense laser in plane geometry. The "i" is the mesh number of Lagrangian hydrodynamic simulation

At i = 100 and 80, the radiation is generated inside the heating region and propagates to the rear direction. The radiation generated laser irradiation is penetrated into deep region with a peaking to the normal direction, since the radiation going to the oblique direction is absorbed by the plasma. As the result, near the rear of the gold target i = 20, radiation flux remains around the normal direction.

Different from the electron transport, there is no angle scattering to make the distribution function relatively uniform. It is known that Thomson scattering makes the photon angular distribution uniform, while as is estimated in Vol. 1, it is almost negligibly small compared to the absorption. It is also known that photons are scattered by Compton scattering, while it becomes effective for the photon with energy comparable to mc^2 and it can be neglected. Of course, the emission term in (7.3) is uniform over the angle and it is expected that the photon distribution is rather uniform over angle for optically thick plasma, $\tau_\nu \gg 1$.

It is useful to compare the difference of transport kinetic between electrons and radiations.

1. The propagation velocity is different in electrons (v), while it is the same in radiation (c).
2. The electron orbit is modified by electric field (E), while radiation propagates straight.
3. Electron collision term is a smooth function of electron energy, while the opacity and emissivity vary over orders of magnitude by bound-bound transition effect.
4. Nonlocal transport of electrons approximately adopts Maxwell distribution as local function, while it is meaningless to assume Planck radiation in laser plasma, because the photon filed is far from LTE even the matter is near LTE.
5. The calculation of spectral opacity and emissivity is very hard and we need to use an approximated atomic model so that it is simple but appropriate to the problem.

7.2 Multi-group Diffusion Model for Radiation Transport

It is also fine to expand the angular distribution by Legendre function as in the case of electron transport. It is, however, noted that due to the lucky property of the collision operator we could eliminate the derivative to μ with use of the relation (6.52) and this is the reason why Legendre expansion is used for angular distribution. In the case of radiation, the angular distribution will be considered later after the formulation of angle moments. We derive the equations to the spectral radiation energy density E^ν and radiation flux density $\mathbf{F}^\nu$ as follows. Integrating (7.3) with the angle d$\mathbf{\Omega}$, we can obtain the equation for radiation energy density;

$$\frac{\partial}{\partial t}E^\nu + \nabla \boldsymbol{F}^\nu = 4\pi\eta^\nu - c\chi^\nu E^\nu \tag{7.11}$$

where E^ν and $\mathbf{F}^\nu$ are defined as

$$E^{\nu} = \frac{1}{c}\int_{4\pi} I^{\nu} d\Omega \tag{7.12}$$

$$\boldsymbol{F}^{\nu} = \int_{4\pi} I^{\nu}\boldsymbol{\Omega} d\Omega \tag{7.13}$$

where $d\Omega = 2\pi sin\theta d\theta = 2\pi d\mu$. We need the equation to $\mathbf{F}^{\nu}$ and it is derived by integrating (7.3) after scalar product with $\boldsymbol{\Omega}$.

$$\frac{1}{c^2}\frac{\partial}{\partial t}\boldsymbol{F}^{\nu} + \nabla \boldsymbol{P}^{\nu} = -\chi^{\nu}\boldsymbol{F}^{\nu} \tag{7.14}$$

where we have new function $\mathbf{P}^{\nu}$ defined as

$$\boldsymbol{P}^{\nu} = \frac{1}{c}\int \boldsymbol{\Omega}\otimes\boldsymbol{\Omega} \mathrm{I}^{\nu} d\Omega \tag{7.15}$$

This corresponds to radiation pressure tensor. In (7.14) the i-th component is

$$(\nabla \boldsymbol{P}^{\nu})_i = \frac{\partial}{\partial x_k} P^{\nu}_{ki}, \quad P^{\nu}_{ki} = \frac{1}{c}\int \Omega_k \Omega_i I^{\nu} d\Omega \tag{7.16}$$

Here, let us introduce angular distribution of radiation intensity. For simplicity, consider the plasma is plane geometry and system is one dimension in x-direction in space. The angular distribution is only the function of θ and assume to be given as $\psi^{\nu}(\theta, x)$. The local radiation intensity is given as

$$I^{\nu}(t, x, \Omega) = I^{\nu}_0(t, x)\psi^{\nu}(\theta, x) \tag{7.17}$$

where $\psi^{\nu}(\theta, x)$ is normalized as

$$\int_{4\pi} \psi^{\nu}_{(\theta,x)} d\Omega = 4\pi, \qquad \int_{-1}^{1} \psi^{\nu} d\mu = 2 \tag{7.18}$$

Then, we obtain the following relation

$$E^{\nu} = \frac{4\pi}{c} I^{\nu}_0, \qquad F^{\nu} = \frac{c}{2} E^{\nu} \int_{-1}^{1} \psi^{\nu} \mu d\mu \tag{7.19}$$

The radiation pressure is given as

$$\boldsymbol{P}^{\nu} = \begin{pmatrix} P^{\nu} & 0 & 0 \\ 0 & P^{\nu} & 0 \\ 0 & 0 & P^{\nu} \end{pmatrix} + \frac{1}{2}\begin{pmatrix} 0 & 0 & 0 \\ 0 & E^{\nu} - 3P^{\nu} & 0 \\ 0 & 0 & E^{\nu} - 3P^{\nu} \end{pmatrix} \tag{7.20}$$

where the scalar pressure P^{ν} is related to the energy density in the form.

$$P^{\nu} = \frac{1}{2} E^{\nu} \int_{-1}^{1} \mu^2 \psi^{\nu} d\mu \tag{7.21}$$

Note that for isotropic distribution ($\psi^{\nu} = 1$), the relation $P^{\nu} = 1/3E^{\nu}$ is satisfied and the pressure becomes scalar in (7.20).

Consider a simple case of one-dimensional plane geometry in real space x. Then, all variables become scalar and the following two equations should be solved self-consistently for each group of radiation energy $h\nu$.

$$\frac{\partial}{\partial t} E^{\nu} + \frac{\partial}{\partial x} F^{\nu} = 4\pi\eta^{\nu} - c\chi^{\nu} E^{\nu} \tag{7.22}$$

$$\frac{1}{c^2} \frac{\partial}{\partial t} F^{\nu} + \frac{\partial}{\partial x} P^{\nu} = -\frac{\chi^{\nu}}{c} F^{\nu} \tag{7.23}$$

To solve (7.3) as precise as possible in general, we need to solve angular distribution with many freedoms, while we have remained only two lowest moment to μ (μ^0 and μ^1) as shown above. Historically, there have been a variety of trial on how to truncate the higher moment with a proper physical model.

If we have a certain relation between the second moment P^{ν} and E^{ν} and F^{ν}, it is possible to truncate the higher moment equations. For example, (7.21) has a form.

$$P^{\nu} = f^{\nu} E^{\nu} \tag{7.24}$$

where the coefficient f^{ν} is defined as

$$f^{\nu} = \frac{1}{2} \int_{-1}^{1} \mu^2 \psi^{\nu} d\mu \tag{7.25}$$

It is clear that the following relations should be satisfied at two extreme situations.

$$f^{\nu} = \begin{cases} 1/3 & \psi_{\nu} = 1 \\ 1 & \psi_{\nu} = 2\delta(\mu - 1) \end{cases} \tag{7.26}$$

In the diffusion limit as the case of Spitzer-Harm in the electron transport, the angular distribution for all frequency is approximated near unity, namely, $\psi_{\nu} \approx 1$. Then, the time derivative to F^{ν} in (7.13) is neglected and $f^{\nu} = 1/3$ is used to obtain the relation.

$$F^{\nu} = -\frac{c}{3\chi^{\nu}} \frac{\partial}{\partial x} E^{\nu} \tag{7.27}$$

Inserting (7.27) into (7.22), a diffusion type transport equation is obtained.

In the case of further ideal case such as optically thick plasmas, for example, the plasma inside the Sun, the radiation energy distribution is near Planckian. In such a case, solving (7.11) and (7.14) is relatively easy and they are altered to Planck

averaged equation with diffusion term for the radiation temperature T_r [2]. Then, the radiation transport is coupled to hydrodynamic equations relatively easily.

As seen in the electron transport, the diffusion approximation is valid only for the case where a typical scale of change L^ν of each frequency is much longer than the mean free path $l^\nu = 1/\chi^\nu$ in (7.27). Eddington has introduced so-called **Eddington coefficient** to limit the flux of diffusion with the form.

$$F^\nu = \frac{R^\nu}{1+R^\nu} cE^\nu \tag{7.28}$$

$$R^\nu = \frac{l^\nu}{3}\left|\frac{1}{E^\nu}\frac{\partial}{\partial x}E^\nu\right| \tag{7.29}$$

where the sign of F^ν is of course the negative gradient direction of E^ν. Note that (7.28) is the same property as the flux limited diffusion of electron transport 7.53).

In laser-produced plasmas, it is not realistic in most of cases to assume the plasma is optically thick to all frequency and the radiation energy distribution is far from the Planckian distribution. Therefore, depending on a problem, we have to decide energy grouping and use or produce the spectral opacity and emissivity based on a certain atomic model and ionization model. This is a tuff job as partially discussed in Chap. 5 and will be discussed later about opacity calculation.

Modeling the coefficient f^ν was initially done by Eddington and his model is called **Eddington factor**. Now, it is widely used an improved Eddington factor based on maximum entropy method [3]. Defining R_1 as

$$R_1 = \left|\frac{F^\nu}{cE^\nu}\right| \tag{7.30}$$

Then, a computer fitted functional form of Eddington factor is shown in the for [3].

$$f^\nu = \frac{1}{3} + \frac{0,.01932R_1 + 0.2694R_1^2}{1 - 0.5953R_1 + 0.02625R_1^2} \tag{7.31}$$

It is clear that this Edington factor smoothly change from 1/3 ($R_1 = 0$) to 1 for ($R_1 = 1$). Since (7.31) varied as a function of R_1, it is also called a **variable Edington factor** and widely used in radiation transport simulations.

It is important to note how the Edington factor is calculated in multi-dimensional space. In Fig. 7.2, a simple example is shown in (x, y) two-dimensional space. In the original paper by Minerbo [3], the formulation is for general case to be used for three-dimensional case and it is derived that the Edington factor becomes the following matrix form for each frequency ν.

$$\boldsymbol{f} = \frac{1}{2}\left(1 - \frac{m_2}{m_1}\right)\boldsymbol{I} + \frac{1}{2}\left(3\frac{m_2}{m_1} - 1\right)\frac{\boldsymbol{F}\otimes\boldsymbol{F}}{|\boldsymbol{F}|^2}, \tag{7.32}$$

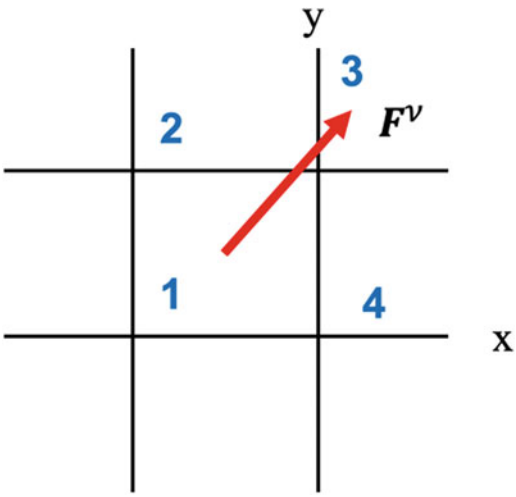

Fig. 7.2 A computational grid in two-dimensional space and a local heat flux vector of the spectral radiation energy. The numbers identify each zone in the simulation meshes

m_1 and m_2 are given in (2.10) in [3]. Note that f is in general a matrix, the first term in RHS in (7.32) is a diagonal term and the second term is a matrix. In Fig. 7.2, for two-dimension, the radiation energy in the numerical discrete zone 1 diffuses to the region 2 and 4 with the matrix in (7.24) with the matrix Edington factor in (7.32). Then, the energy diffuses to the zone 3 from zones 2 and 4. With such two-step diffusion, the energy in zone 1 is transferred to the zone 3 as we expected. For only the case of one-dimension (7.32) tends to a scalar as in (7.31).

7.3 Modeling Spectral Opacity and Emissivity

Radiation transport kinetics is relatively simple compared to the electron transport, because the photon velocity is the speed of light, its orbit is strait, and we can neglect the change of the photon energy by Compton scattering etc. in laser plasmas. However, another difficulty appears in calculating the spectral opacity and emissivity, η^ν and χ^ν. In the case of fully ionized plasma, both are continuous spectra and are given as Bremsstrahlung process shown in Chap. 5.

So, studying radiation phenomena in magnetic confinement fusion plasma, the fuel hydrogens can be assumed to be fully ionized and total emissivity provides the radiation loss from core plasma. This is also the case of very early universe where the space is full of only hydrogen and helium and the ionization and recombination is easy to be studied. It is known that after the recombination at about 400,000 years after the Big Bang, the photons decoupled with the atoms and its Planckian distribution is now observed as Cosmic Microwave Background (CMB) of T = 3 K. However, it is known that re-ionization occurs by ultra-violet photons generated by the first-generation stars after the gravitational attraction. The radiation from each

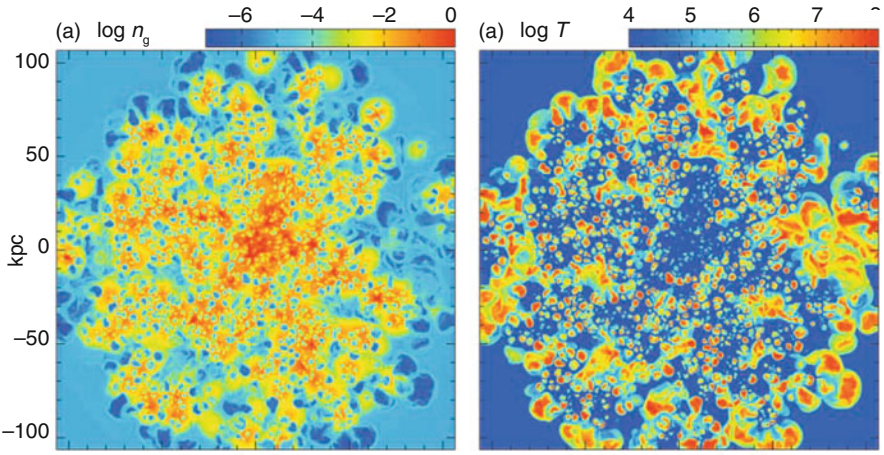

Fig. 7.3 Numerical simulation of radiation transport and star formation in a forming galaxy. Reprinted with permission from Ref. [4]. Copyright by American Astronomical Society

star perturbs the clouds to trigger the formation of new stars. In Fig. 7.3, numerical results at 50 million years on the multiple supernova explosions in a forming galaxy are shown, where (a) the density and (c) temperature distributions are shown over the space of 200 kpc (~0.6 million light years) [4]. Such simulation demands precise treatment of radiation kinetics over full angle and directions.

In solving photo-ionization process, the opacity and emissivity due to the electron transition between bound state to free state should be modeled in the opacity and emissivity. Both spectral properties are reflection of the cross sections discussed in Chap. 5.7. They are continuous spectrum with the edges by the ionization potential. Inclusion of spectral opacity and emissivity of bound-bound transitions is in general hard task. Since the laser can be irradiated any material, especially solid targets with relatively mid-Z to high-Z atoms. Even with intense lasers, they cannot be fully ionized abruptly and radiation transport in partially ionized plasma becomes important as energy transport non-locally.

In Fig. 7.4, emission spectrum is shown for carbon plasma at a temperature of 50 eV and density of 4.3×10^{-3}g/cm^3 [5]. The locations of 1s ionization thresholds of C III, C IV, and C V are indicated by arrows. It is clear that three different codes give almost the same spectra, while the line emissivity spectra are different. Fig. 7.4 suggests that the emitted line radiations are absorbed in plasma even relatively small plasma. If such line transport becomes important in a given plasma, we are demanded to model such line radiation with a reasonable model to grasp the essence of the physics.

As shown in Fig. 7.4, the ionization energies of 1s in different charge states make the emission edges at different energies of photons. Before calculating the spectral emissivity and opacity, we have to calculate the atomic data of all ionization states.

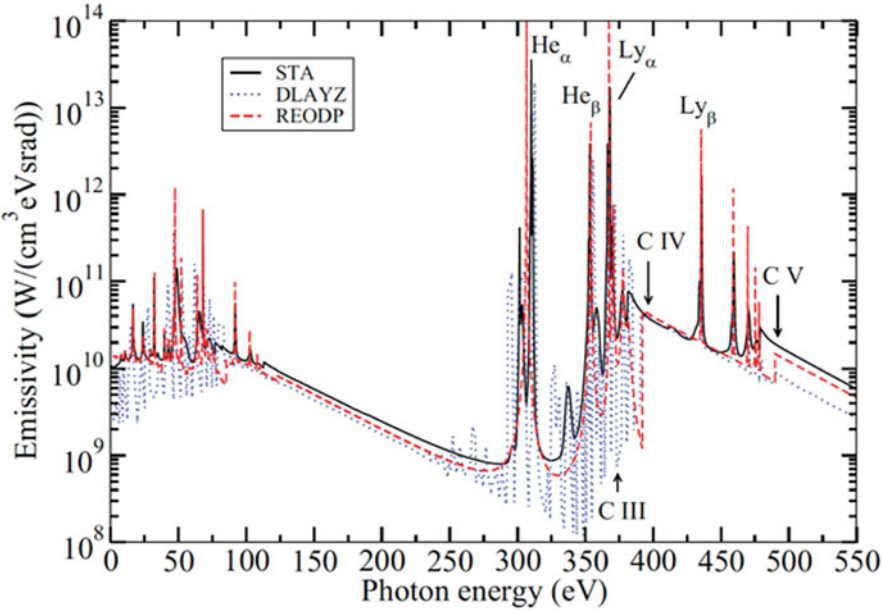

Fig. 7.4 Emission spectra from three different codes are shown for carbon plasma at a temperature of 50 eV and density of 4.3×10^{-3} g/cm^3. Reprint with permission from Ref. [5]. Copyright 1998 by American Physical Society

As shown in Chap. 5.3, there are several precise models to obtain the atomic data for any configurations. Ab initio calculation requires to obtain the distribution of atomic configurations for all charge states. It is clear to carry out such calculation itself very hard task. So, depending on the physics we want to study, some simplification is always recommended.

Assume that we are able to calculate the data base of all configurations of all charge state atoms. Then, we can use **Saha equation** in Sect. 5.2 to obtain the distribution of all configurations of ions in LTE plasma. In Fig. 7.5, the distribution of Si charge states is shown for the cases of temperatures of 100, 50, and 25 eV for silicon dioxide (triangles) and pure silicon (squares) [6]. The density of the plasma is 45 mg cm^{-3}. The ion charge state is calculated with Saha equation and the atomic states of partially ionized silicon ions are modeled with the **detail level accounting (DLA)** where the energy levels are calculated with Hartree-Hock method for many possible configurations as the data base for Saha equation. In Fig. 7.5, it is seen that about $4 \sim 5$ different charge states coexist in a state. Most of they are expected to be at the ground state configurations, while the contribution by excited ions cannot be neglected.

In order to see how detail configuration should be included in calculating opacity from such plasma, the opacity spectrum is calculated by including the following configurations to each charge state ion.

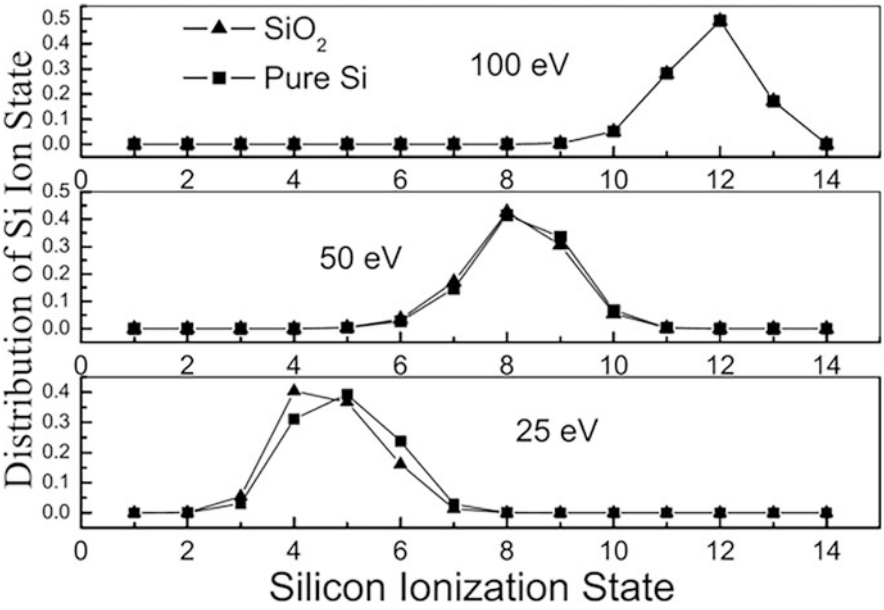

Fig. 7.5 The distribution of Si charge states is shown for the cases of temperatures of 100, 50, and 25 eV for silicon dioxide (triangles) and pure silicon (squares). Reprinted with permission from Ref. [6]. Copyright by American Astronomical Society

$$1s^2 2l^m, \quad 1s^2 2l^{m-1} n'l', \quad 1s^1 2l^{m+1}, \quad 1s^1 2l^m n'l',$$

where $n' < 8$, $l' < n'$ in the DLA calculation. In Fig. 7.6, the resultant opacity spectrum is plotted by varying the maximum of n'. The solid, dashed, dotted, and dash-dotted lines represent models with maximum principal quantum numbers of 8, 6, 4, and 2, respectively. All four models were calculated with the same temperature (56 eV) and density (10 mg/cm^3). The only difference is the number of levels used in each model. From this figure, it is clear that the absorption features become deeper with the inclusion of more levels. However, the absorption changes slightly with increase of n'. For example, in the calculations shown in Fig. 7.6 about 70% of the absorption is attributed to the level n' = 2, and 20% is due to the levels with n $'$ = 3–6. The contributions to the absorption from levels n$'$ = 7 and n$'$ = 8 are only about 10%, and the contribution from level n$'$ = 8 is even less than 5%.

In order to understand which transitions are contributing each spiky spectrum of opacity, consider the calculated transmission spectra of the silicon plasma under almost the same temperature and density as in Fig. 7.6 [7]. In Fig. 7.7, the spectra are shown for the higher photon energy so that the transition is simpler to be explained. The ionization state (Z*) distribution is like that for 50 eV in Fig. 7.5, and most abundant ions are Z* = 6 to 10, corresponding to O, N, C, B, and Be-like silicon, respectively. The transmission (opacity) spectrum due to each charge state silicon is shown in Fig. 7.7. The spectrum of "All ions" is the sum of all from each charge state ions, where the solid line is the theoretical and dotted line is the experimental data [7].

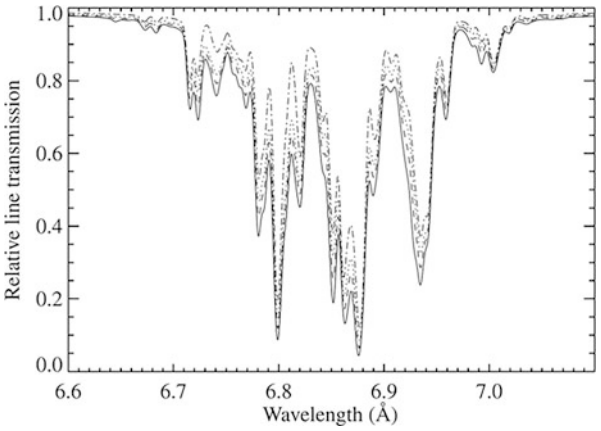

Fig. 7.6 The resultant opacity spectrum with DLA calculation is plotted by varying the maximum of n'. The solid, dashed, dotted, and dash-dotted lines represent models with maximum principal quantum numbers of 8, 6, 4, and 2, respectively. All four models were calculated with the same temperature (56 eV) and density (10 mg/cm^3). Reprint with permission from Ref. [7]. Copyright 1998 by American Institute of Physics

It is informative to know which transitions of ion configurations contribute to each of sharp opacity spectrum. It is seen that the Be, B, and C-like ions make two absorption peaks. It is found that the lower energy part is due to the inner-shell transition in n = 2, while the higher energy is the transition to higher n shell. For example, the dashed line of B-like is the result when the maximum configuration is n = 2 in DLA calculation. Let us see the transitions in B-like ion. The inner shell transition is from the ground state to the following transitions.

$$1s^2 2s^2 2p^1 \rightarrow 1s^2 2s^1 2p^2 \rightarrow 1s^2 2p^3$$

On the other hand, the higher energy peak in C-like ion is given by the transition.

$$1s^2 2s^2 2p^1 nl \rightarrow 1s^2 2s^1 2p^2\ nl \rightarrow 1s^2 2p^3 nl$$

where $n \geq 3$ *and* $l < n$. Such an electron in (n, l) is called a satellite electron which contribute to a small modification of absorption spectrum from the above transition, consequently such transition energy is almost the same position as the lower one of B-like as in Fig. 7.7.

In calculating Figs. 7.6 and 7.7, LTE has been assumed to a uniform plasma heated by thermal radiation generated in a gold cavity heated by intense laser [6]. However, it is not in general to be valid to use LTE assumption, especially laser ablating plasma from medium and high Z targets. Then, some non-LTE distribution should be calculated for charge state distribution of plasma in calculating emissivity and opacity. A better model is **collisional radiative equilibrium** (CRE) model for the case of relatively small plasma characterized by the radiation field is much less compared to Planck radiation. Most of the opacity and emissivity of high-temperature laser plasma and other laboratory plasma probably calculated with charge distribution with CRE model.

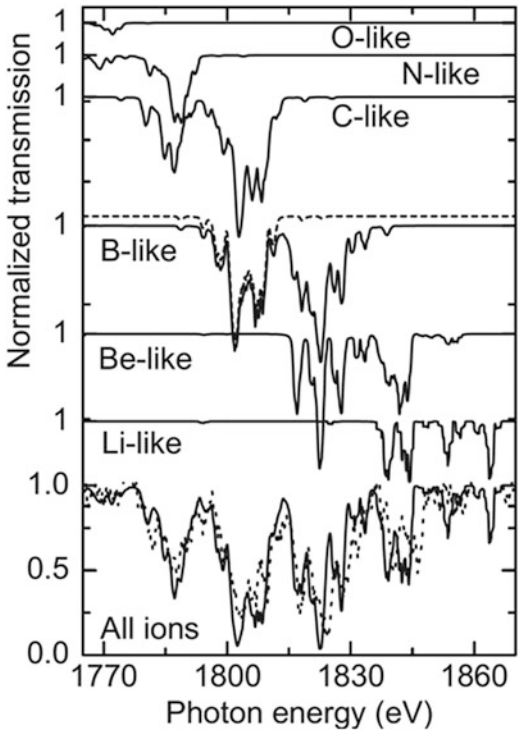

Fig. 7.7 Transmission spectra due to different configuration of partially ionized ions. The solid lines are theoretical and the dotted line is experimental. Reprint with permission from Ref. [7]. Copyright 1998 by American Institute of Physics

In dense plasmas produced by intense lasers, we can expect the line broadening [8]. the melting of nearby lines to make a kind of band structure. Then, spectral opacity looks easier to model in computer simulation of radiation transport. In Fig. 7.8, the emissivity of carbon plasma with T = 100 eV at five different densities is plotted [5]. It is clear that the lines become broader due to mainly **Stark broadening** effect. It is seen nearby lines melt to finally becomes broad spectrum seen for the density 22.4 g/cm^3. Note that the disappearance of the lines near the ionization edge, say near 500 eV as the density increases is due to the **pressure ionization** effect to be discussed in Chap. 8.

It is useful to see how bound-bound transition opacity is important in plasma even with small number of high-Z atoms. This is the case of the opacity inside the Sun. The sound velocity distribution of the plasma in the Sun has been studied precisely with the helioseismology and its theoretical study requires opacity and self-consistent equation of state [9]. For example, around the boundary of convection and radiation zones roughly characterized with T = 193 eV and $n_e = 10^{23}$ cm^{-3}, the opacity of partially ionized iron is plotted in Fig. 7.9 [10]. It is clear that photo-excitation (red) by bound-bound transition is dominant over 600–1000 eV where the radiation intensity is near peak $h\nu = 2.8$ T ~ 600 eV. In addition, it has fine structure spectra. The photo-ionization (green) by bound-free transition also contributes substantially. The inverse-Bremsstrahlung (blue) by free-free transition is relatively

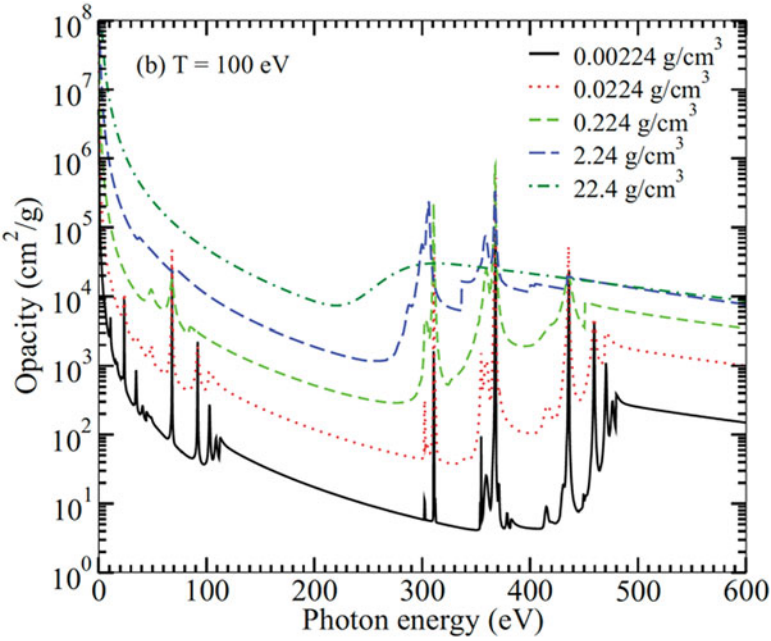

Fig. 7.8 Emission spectrum of carbon plasma at T-100 eV with five different densities are plotted. Reprint with permission from Ref. [5]. Copyright 1998 by American Physical Society

small. In general, we can neglect the effect of scattering (pink) in non-relativistic plasmas.

7.4 Opacity Experiments

Using intense laser or laser-produced or pulse-power produced thermal radiation, spectral transmission **opacity experiment** has been carried out and compared the data to computational results [11]. This is a clear validate and verification research on complicated opacity of high density and high temperature plasmas. Opacity experiment is important not only for radiation transport in laser produced plasma but also for a variety of topics in astrophysics, especially stellar evolutions [9]. Let us briefly see the present status of the opacity experiment and the code comparison.

The stellar interior is characterized with high-density and high-temperature and it is well known that the radiation transport is important to transfer the nuclear fusion energy near the center of a star toward the surface, such as the Sun. The structure of stars strongly depends on the atomic state of the plasma inside the stars. Historically, the opacity has been calculated theoretically, especially using computers. After the progress of intense laser and Z-pinch facilities, a variety of spectroscopic opacity

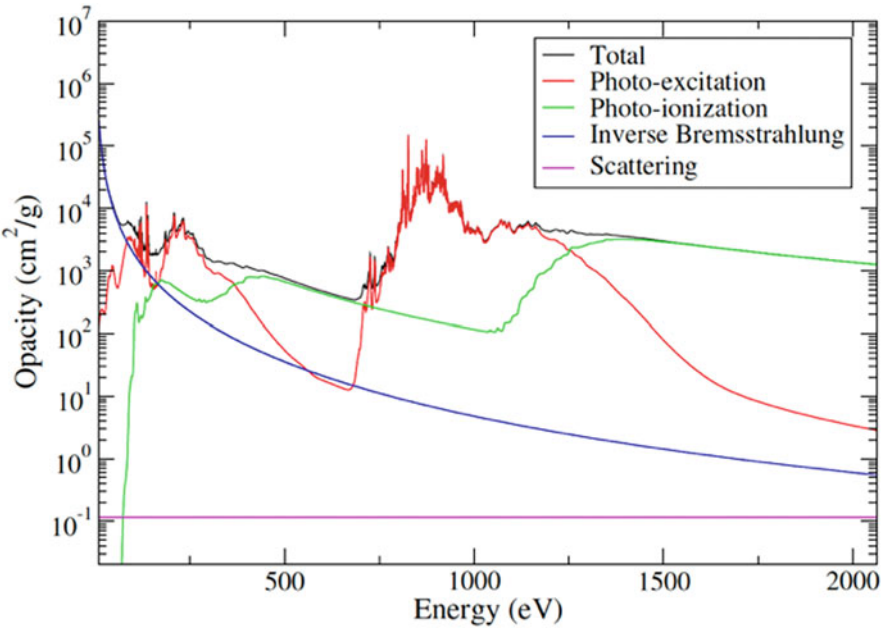

Fig. 7.9 The opacity of the plasma of the Sun around the boundary of convection and radiation zones roughly characterized with T = 193 eV and $n_e = 10^{23}$ cm^{-3} [10]

experiments have been performed [12, 13]. Inside of stars, heavy elements like iron are of very small fraction, while it contributes the opacity significantly.

Iron contributes significantly to solar opacity; the relatively large number of bound electrons makes iron more susceptible to model uncertainty of the standard solar model. It is found that opacity model predictions were lower than the opacity data when the temperatures and densities were increased to solar interior values [13].

Precise experiments with Z-facility have been done for Cr, Fe, and Ni to consider the atomic physics causing the lower opacity in Fe plasma [14]. In Fig. 7.10, the experiment setup is shown in (a). Almost Planck radiation of 350 eV radiation temperature is generated by Z-pinch (radiation source) and is irradiated to a plane target with aa half-site opacity sample covered by Be and CH optically thin solids shown in (b). The radiation spectra transmitted through both layers measured by crystal spectrometers are compared to obtain the transmission spectrum to reduce to the spectral opacity. In the experiments, the temperature and electron density measurements result the sample plasma being 180 eV and 3×10^{22}cm^{-3}. In (c), dominant electron configurations of Cr, Fe, and Ni at achieved conditions are shown. Vacancies in the shells are indicated by open circles.

In Fig. 7.11, the experimental opacity is compared to the calculation with OP opacity code. The OP opacity model is widely available and extensively used for solar or stellar models [14]. Comparisons between OP and the measured opacities provide essential clues for model refinements. It is clear in Fig. 7.11 that Cr and Ni opacities are well

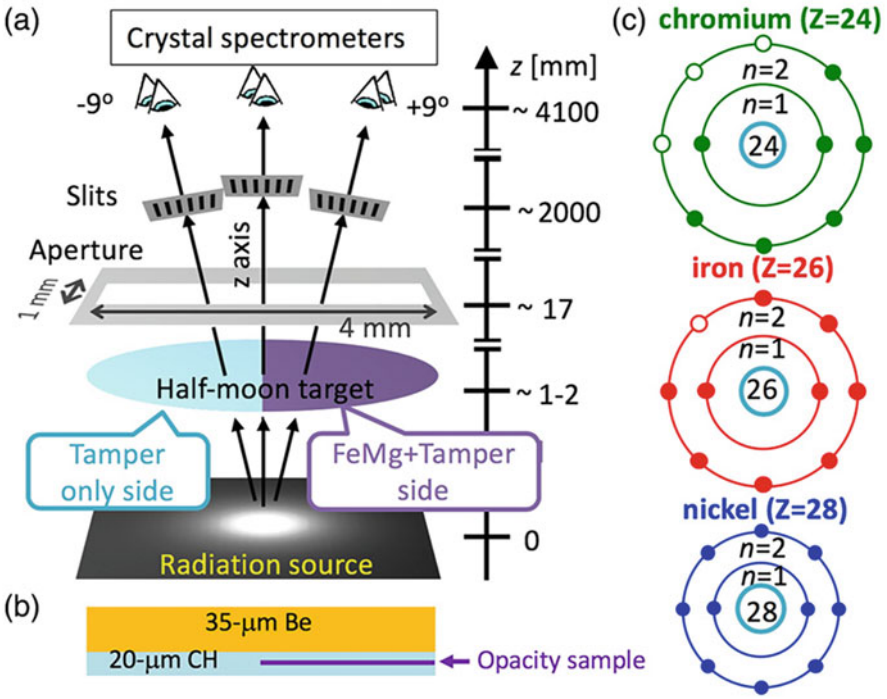

Fig. 7.10 The experimental set up to measure the opacity of chromium, iron, and nickel. Reprint with permission from Ref. [14]. Copyright 1998 by American Physical Society

modeled, while a large discrepancy is seen for Fe. It is about a factor two near 7–8 A region. As seen in Fig. 7.11 (c), Fe ion has open-shell and it is expected there are many lines absorption by the term splitting, which is probably not well included in OP code. The difference of the line positions and line shapes is studied in [14]. It is reported that the other modern atomic codes can improve such discrepancy.

The discrepancy of Fe opacity is very critical especially for astrophysics, because iron is rich abundance in the universe. The higher-than-predicted iron opacity data account for about half the increase needed to resolve the standard solar model discrepancy. This question is critical because, if the data are correct, our understanding of photon absorption in high-density matter must be revised. This would have far-reaching consequences for astrophysics and terrestrial science.

For example, a widely used method to estimate stellar ages depends on opacity, and opacity revisions will therefore lead to substantial changes in the age estimates. Furthermore, if solar composition, opacity, and helioseismology inferences are found to be consistent, the soundness of the **standard solar model** will be reinforced, but the composition and opacity used to model other Sun-like stars must be revised. On the other hand, if observations and solar model inputs cannot be reconciled, possible modifications to the solar model itself would be necessary. A

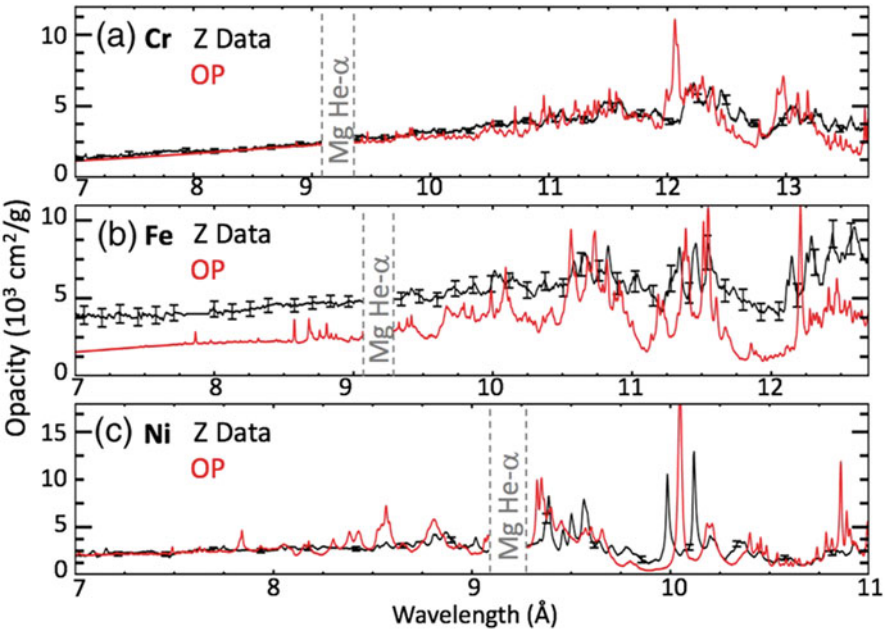

Fig. 7.11 Comparisons between OP opacity code and the measured opacities of three plasma samples. Reprint with permission from Ref. [14]. Copyright 1998 by American Physical Society

new theory, for example, has been proposed to explain the enhanced opacity by taking account of two-photon absorption effect [15].

Of course, the opacity is one of the most important elements to model stellar evolution. The consensus model for a classical nova invokes a binary star system, with accretion from a main-sequence star or evolved giant onto a white dwarf (WD) due to Roche lobe overflow. As hydrogen-rich material is transferred to the WD through an accretion disk, the temperature at the base of the accreted envelope rises until it reaches $\sim 2 \times 10^7$ K, at which point the accreted fuel undergoes fusion via the CNO cycle. A convective zone is born and grows until an optically thick wind is launched, giving rise to the observed classical nova. The launching of the optically thick wind is primarily due to the presence of the iron opacity bump. Accurate opacity of iron is essential to compare observation light cure to a theoretical model [16].

7.5 Radiation Hydrodynamics

The hydrodynamic description of the system consisting of huge number of particles is widely used in many cases from design of air-conditioning to astrophysics, even in cosmology. In laser produced plasmas, they are described in general with two-temperature, one-fluid model as shown in Chap. 2.6. For the fluids being in

LTE with the density ρ, velocity **u**, and internal energies of the ion fluid ε_i and electron fluid ε_e, (2.105, 2.106, 2.107, and 2.108) should be solved in time and space, where the energy flows to the ion and electrons local fluids are given.

It is convenient to show (7.22) and (7.23) in Lagrangian frame moving with the plasma fluid. By use of (2.105) and (2.106), it is easy to show the equations of radiation in the fluid frame,

$$\rho \frac{d}{dt}\left(\frac{E^\nu}{\rho}\right) + \nabla(\boldsymbol{F}^\nu - \boldsymbol{u}E^\nu) = 4\pi\eta^\nu - c\chi^\nu E^\nu \tag{7.33}$$

$$\frac{\rho}{c}\frac{d}{dt}\left(\frac{\boldsymbol{F}^\nu}{\rho}\right) + \nabla\left(c\boldsymbol{P}^\nu - \frac{\boldsymbol{u}}{c}\otimes\boldsymbol{F}^\nu\right) = -\chi^\nu \boldsymbol{F}^\nu \tag{7.34}$$

Note that the right-hand-sides in (7.33) and (7.34) are contribution via the coupling with the plasma fluid and they will couple with the equations of energy and momentum of plasma fluid, respectively.

From (2.105), (2.106) and (7.34), the following equation of fluid motion is obtained.

$$\frac{\partial}{\partial t}(\rho\boldsymbol{u}) + \nabla(\rho\boldsymbol{u}\otimes\boldsymbol{u} + \mathrm{P}) = \boldsymbol{S}_r^m \tag{7.35}$$

where $\boldsymbol{S}_r^m$ is the momentum change of the fluid due to the absorption of radiation added to (2.106) as the coupling term in (7.34). The form of $\boldsymbol{S}_r^m$ is derived from 7.34) as

$$\boldsymbol{S}_r^m = \frac{1}{c}\int_0^\infty \chi^\nu \boldsymbol{F}^\nu d\nu \tag{7.36}$$

Note that no momentum change appears due to the radiation emission, because it is assumed to be isotropic. The energy conservation relation to the electron fluid is also obtained after simple mathematics and it is found to be

$$\frac{\partial}{\partial t}\left(\rho\varepsilon_e + \frac{1}{2}\rho u^2\right) + \nabla\left[\rho\boldsymbol{u}\left(\varepsilon_e + \frac{P}{\rho} + \frac{1}{2}u^2\right)\right] = S_r^\varepsilon \tag{7.37}$$

where $\boldsymbol{S}_r^\varepsilon$ is the cooling and heating terms due to the radiation. The form of $\boldsymbol{S}_r^\varepsilon$ is given from (7.33) as

$$S_r^\varepsilon = \int_0^\infty (c\chi^\nu E^\nu - 4\pi\eta^\nu)d\nu \tag{7.38}$$

When the fluid and radiation are treated as one system, the total momentum and energy conservation relations are obtained from (7.34) and (7.35), and (7.33) and (7.37) as follows, respectively.

$$\frac{\partial}{\partial t}\left(\rho \boldsymbol{u} + \frac{\boldsymbol{F}^R}{c^2}\right) + \nabla\left(\rho \boldsymbol{u}\otimes\boldsymbol{u} + \mathrm{P} + \boldsymbol{P}^{\mathrm{R}}\right) = 0 \tag{7.39}$$

$$\frac{\partial}{\partial t}\left(\rho\varepsilon_e + \frac{1}{2}\rho u^2 + E^R\right) + \nabla\left[\rho \boldsymbol{u}\left(\varepsilon_e + \frac{P}{\rho} + \frac{1}{2}u^2\right) + \boldsymbol{F}^R + \boldsymbol{q}^e\right] = 0 \tag{7.40}$$

where E^R, $\boldsymbol{F}^R$, and $\boldsymbol{P}^R$ are spectrum integrated total values of E^ν, $\boldsymbol{F}^\nu$, and $\boldsymbol{P}^\nu$, respectively. For simplicity, the last two terms in RHS in (2.108) are neglected in (7.40). The electron heat flux $\boldsymbol{q}^e$ has been discussed in Chap. 6 and the nonlocal and multigroup flux of SNB given in (6.91) is recommended to be used to evaluate the electron hear flux in a better way, not like Spitzer-Harm diffusion shown in (2.109).

Let us evaluate how important the four radiation terms in (7.39) and (7.40) in the case of laser-produced plasmas. In evaluating each radiation term, it is assumed that the radiation heat flux is important to affect the hydrodynamic energy flux and the following rough relation is applied.

$$F^R \sim O(uP), \quad E^R \sim O\left(\frac{F^R}{c}\right), \quad P^r \sim O\left(E^R\right), \tag{7.41}$$

where "O" means the order of magnitude. Compare the radiation term to the fluid term in each parenthesis.

$$\frac{F^R}{c^2\rho u} \sim O\left(\frac{u^2}{c^2}\right), \qquad \frac{P^R}{P} \sim O\left(\frac{u}{c}\right), \quad \frac{E^R}{\rho\varepsilon_e} \sim O\left(\frac{u}{c}\right) \tag{7.42}$$

As far as the plasma is non-relativistic fluid, all radiation terms except the radiation heat flux in the energy flux density in (7.40) can be neglected in general.

It is interesting to note the case where the plasma fluid is not non-relativistic while another radiation term(s) become important. For example, inside stars the radiation mean free path is very short and the radiation is almost Planckian distribution. Since the radiation pressure and energy density is proportional to T^4 while the those of plasma particles are in proportion to T, there is critical temperature to a given density that the radiation pressure is comparable to the pressure by the matter. In such a case, we have to keep all radiation terms in radiation hydrodynamic equations. The reason why the above order estimate was wrong inside the stars is as follows. Inside the stars, almost hydrostatic force balance is a good assumption and the assumption $F^R \sim O(uP)$ in (7.41) is not established. The order estimate in such a case is all O(1) in (7.42). Finally noted that the electron heat transport can be neglected in general

inside stars and it is easy to show because the scale of temperature change is much longer than the charged particle means free paths.

7.5.1 Radiation Pressure

In the case of direct laser irradiation to relatively low Z target, the radiation field is far from LTE and the radiation pressure can be neglected. In the case of high-Z target irradiation or radiation confinement by the hohlraum cavity target, it is not so clear if this condition is valid. Evaluate the relation between pressures by matter and radiation within the assumption that radiation temperature is equal to that of the matter. Radiation energy flux S_P and radiation pressure P_P are given as

$$\begin{aligned} S_P &= \sigma T^4 = 1. \times 10^5 T_{eV}^4 \quad \left[W/cm^2\right] \\ P_P &= \frac{4}{3c}\sigma T^4 = 4.6 \times 10^{-6} T_{eV}^4 \quad \left[J/cm^3\right] \end{aligned} \tag{7.43}$$

As already evaluated, about 300 eV Planck radiation gives the flux of 10^{15} W/cm^2. Then, the radiation pressure P_P is about 0.7 Mbar, which is much less than the material pressure as seen in Chap. 3.

It is of course, radiation pressure becomes larger than the plasma pressure for extremely high temperature or low density. Simple evaluation for the balance is

$$2n_e T = \frac{4}{3c}\sigma T^4 \tag{7.44}$$

For the temperature higher as shown in the relation

$$T_{eV} > 3.8 \times 10^{-5} n_e^{1/3}, \tag{7.45}$$

the Planck radiation pressure is higher than the plasma pressure and radiation hydrodynamics is governed not only the radiation energy flux, but also by the radiation pressure to the matters.

In the evolution of stars, there are cases where high temperature Planck radiation propagates to the surface and the atmospheric matters are blown off as stellar wind. This depends on the metallicity of the star and the mass of the stars. It is useful to note that fate of stars as functions of their initial mass and metallicity. Heger et al. has carried out comprehensive and systematic radiation hydrodynamic simulations including the nuclear reactions [17]. In the abstract, the authors wrote as

> How massive stars die—what sort of explosion and remnant each produces—depends chiefly on the masses of their helium cores and hydrogen envelopes at death. For single stars, stellar winds are the only means of mass loss, and these are a function of the metallicity of the star. We discuss how metallicity, and a simplified prescription for its effect on mass loss, affects the evolution and final fate of massive stars. We map, as a function of mass and

metallicity, where black holes and neutron stars are likely to form and where different types of supernovae are produced. Integrating over an initial mass function, we derive the relative populations as a function of metallicity.

One result is shown in Fig. 7.12, where the horizontal axis is the initial mass of single star divided by the mass of the sun and the vertical axis is the metallicity [17]. The metallicity means how much elements heavier than hydrogen and helium exists. The "metal free" is just after the big bang and the gas is made of only hydrogen and helium, while "abundant solar" is the metal distribution inside the sun. It can be regarded the metallicity means the time evolution of Universe. In Fig. 7.12 the final fate of the stars is shown. The starts with mass more than about ten finally explode as supernova type II (core collapse type). Note that the green line shows the boundary where the hydrogen envelope is blowen off by the strong radiation from the inside, radiation pressure and momentum deposition by Thomson scattering. This is the reason why there is the maximum of the mass of stars about 40 observed in our galaxy as seen in Fig. 7.12 as the green boundary.

The radiation pressure and energy transport are critical physics to control the time evolution of brightness of novae [18]. Because an abrupt ignition of nuclear fusion happens on the surface of white dwarfs due to the increase of temperature by accretion, the surface gas is pushed by the radiation and it is observed that the object suddenly starts to increase the light and finally decays. This is called "nova light curve" and its observation data is analyzed with radiation hydrodynamic simulation code.

7.6 Neutrino Transport in Core-Collapse Supernovae

The kinetics of neutrino transport in core-collapse supernova explosion is the most challenging subject as radiation transport numeric. Neutrino propagates at the speed of light as x-rays in plasma, however, the opacity is simpler than the case of photons. The structure of basic equation is the same as (7.3) and the cross section of the matter interaction $\sigma_\nu(\varepsilon_\nu)$ is relatively simple as given to be

$$\sigma_\nu(\varepsilon_\nu) \sim \left(G_F'\right)^2 \varepsilon_\nu^2$$

$$G_F' = \frac{G_F}{(\hbar c)^3} = 5.3 \times 10^{-44} \ \left[cm^2/MeV\right] \tag{7.46}$$

where G_F is Fermi constant. Since the supernova explosion, the most energetic neutrino has the energy of about 10 MeV and the typical absorption cross section $\sigma_\nu \sim 5 \times 10^{-42}\ cm^2$. This extremely small value is due to that fact that the weak interaction force acts by exchange of heavy W and Z-bosons. Before going to discuss the role of neutrino heating, let us estimate the stopping length of neutrino. The column density of neutrino stopping $(\rho l)_\nu$ is roughly evaluated to be

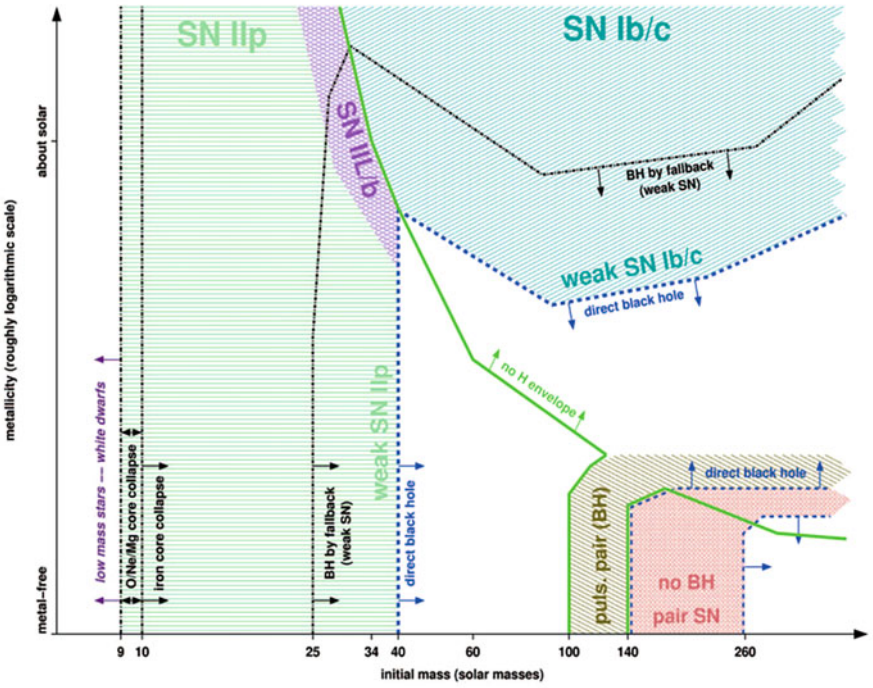

Fig. 7.12 The metallicity dependence of the evolution of stars. The horizontal axis is the initial mass of single star divided by the mass of the sun and the vertical axis is the metallicity. Reprinted with permission from Ref. [17]. Copyright by American Astronomical Society

$$(\rho l)_\nu \sim \frac{m_p}{\sigma_\nu} \sim 4 \times 10^{18} \quad \left[g/cm^2\right] \tag{7.47}$$

As we see below, the size of collapsing core is about 100 km, consequently the matter density is of the order of 10^{10} g/cm^3. It is clear that the earth is transparent to neutrino, because the column density of the earth is about 6000 km × 5.5 g/cm^3 ~4×10^8 $[g/cm^2]$.

It is well-known that the total energy of the neutrino produced by the core-collapse is 10^{53} erg, about 5% of $Mc^2 = 1.8 \times 10^{54}$ *erg* (M: solar mass). Then, only 1% of neutrino energy is absorbed in the core to energize the shock propagation toward the massive star surface. Therefore, it requires very precise analysis of neutrino transport.

Just before the observation of SN1987A, core-collapse supernova explosion has been simulated by Wilson and discussed with Bethe [19]. They obtained the flow diagram in 1-D spherical geometry as shown in Fig. 7.13. The time is second and radius cm units. The iron core of about 1000 km collapses at t = 0 due to the iron dissociation to 13 alpha particles. This nuclear process energy absorption and the pressure drops abruptly to form a proto-neutron star (PNS) of about 10 km. In

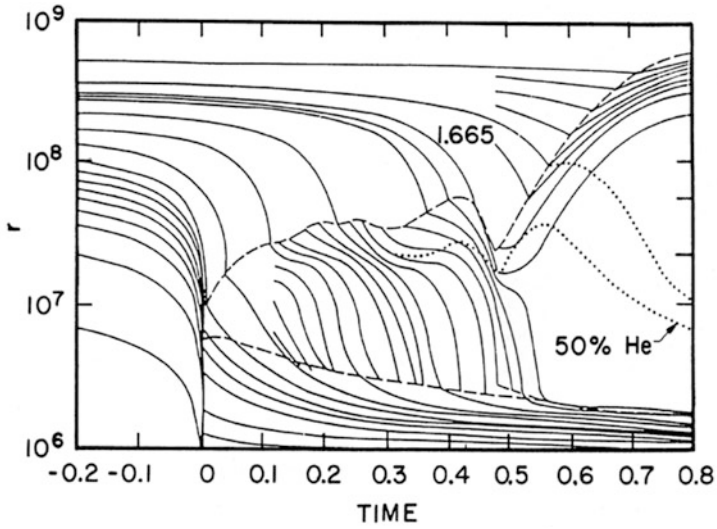

Fig. 7.13 The flow diagram in radius r and time is plotted for gravitational collapsing supernova explosion. The solid lines are flow line indicating time evolution of Lagrangian numerical meshes; the lower dashed curve is the radius of neutrino sphere and the upper one is the out-going shock wave. Reprinted with permission from Ref. [17]. Copyright by American Astronomical Society

Fig. 7.13, the solid lines are flow line indicating time evolution of Lagrangian numerical meshes; the lower dashed curve is the radius of neutrino sphere and the upper one is the out-going shock wave. In the simulation, around 0.48 [s] the **quasi-vacuum region** starts to expand due to the neutrino heating and it is concluded that the shock wave keeps to propagate outward also with neutrino heating. However, it is clear that the quasi-vacuum region accelerates the falling matter outward against the strong gravity is only possible in the constrain of one-dimensional assumption. It is unstable to hydrodynamic instability.

Two years later from the paper of Ref. [19], SN1987A explosion was observed。 The light of the explosion was a physical event for 400 years as a supernova visible to the naked eye. After intensive research on the physics of SN1987A, precise simulations have clarified that two additional physics are critical to modeling supernova explosion. One is the weakening of the shock wave via the iron dissociation at the shock front. Modern simulation has concluded that core-collapse supernova never explodes within one-dimensional geometry; this is due to the fact that the shock wave is weakened by the endothermic effect by the dissociation of falling iron and disappears. The other is the reheating of the core and falling matter via multi-dimensional material mixing is essential to enhance the heating rate by neutrino. Therefore, detail neutrino transport kinetics is required to be simulated in multi-dimensional hydrodynamics.

Typical difficulty of the neutrino transport is schematically shown in Fig. 7.14. Neutrino is generated in proto-neutron-star, where the neutrino is optically thick to

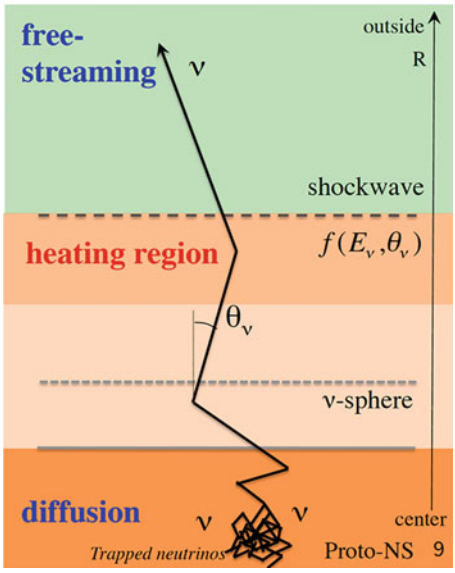

Fig. 7.14 Local to non-local transport model is essential to study the explosion simulation of gravitationally collapsing supernova explosion [Courtesy of K. Sumiyoshi]

diffuse out from the surface and small fraction of energy of about 1% of the total energy is absorbed by the matter to keep and revival the shock wave to propagate outward. The shock wave is important to disassemble the heavy elements toward the space and only the neutron star remains. The kinetics to continue from optically thick to thin region is challenging subject.

The basic equation of neutrino transport is the same as (7.3) with scattering term on RHS. Therefore, the same modeling as in Chap. 7.2 is shown, for example, in [20]. In [20], three different Edington factors are compared, including (7.32) by Minerbo. The transport kinetics of such discrete ordinate method is compared to that with Monte-Carlo method and it is concluded that a good agreement has been obtained in 1-D and 2-D background hydrodynamic structures. Up to now, it is almost concluded that 1-D never explodes and some of 2-D and 3-D simulations gives explosion, but it is not always.

In order to try to solve Boltzmann equation as precise as possible and carry out simulation with the world-class supercomputer, numerical scheme to solve directly the Boltzmann equation to the neutrino energy distribution function in 3-D geometry in space and neutrino angle has been developed and tested in given static fluid structures [21]. The simulation code has been up-graded to run in the K-computer for carrying out self-consistent 3-D radiation hydrodynamic simulation of core-collapse supernova explosion [22].

One case of core-collapse supernova 3-D simulation has been carried out and reported in [22]. The snap shot of t = 10 ms after the collapse is plotted in Fig. 7.15 [22]. The physical quantities in the iso-surfaces of cut away above the equatorial plane in 3-D are shown. The left is contours of entropy (~ temperature) and the arrows with color are average velocities. The orange sphere region is shock heated

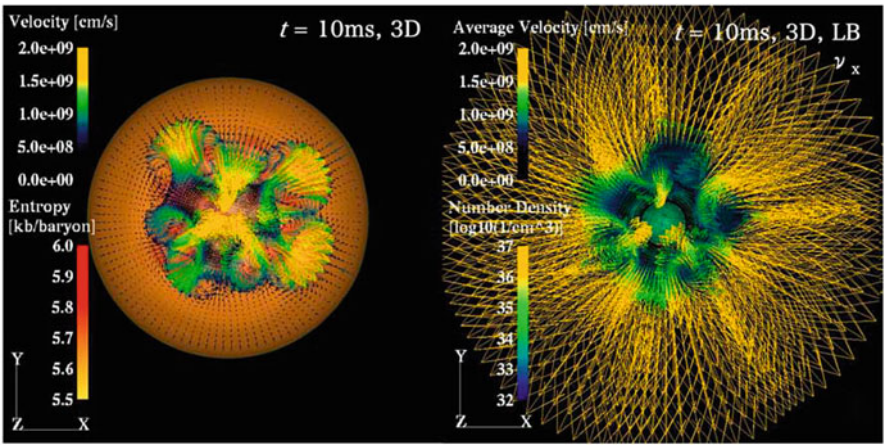

Fig. 7.15 Sophisticated neutrino transport is coupled with three-dimensional hydrodynamic simulation to clarify the physics of supernova explosion. Reprinted with permission from Ref. [22]. Copyright by American Astronomical Society

one and the color boundary is the position of shock wave. Note that fluid explosion velocity reaches almost 10% of the speed of light. The right figure shows a neutrino density contours overlapped with the velocity vectors of local neutrino averaged over the angle; namely, the total neutrino flux velocity of $\langle F/E \rangle$. It is clear that this value ranges from 0 to c place to place. This simulation is not enough to identify the explosion scenario in three-dimensional with precise solver of Boltzmann equation to neutrino. It is expected to clarify the physical condition under which the core-collapse supernova explodes or not by use of the next generation supercomputers. The readers interested in such challenging physics due to neutrino and hydrodynamics can know more in [23] and [24].

References

1. H. Takabe, K. Nishikawa, Computational model for non-LTE atomic process in laser produced plasmas. J. Quanr. Specrrosc. Rad. Transf. **51**, 379–395 (1994)
2. Ya B. Zel'dovich, Yu P. Raiser. Physics of Shock Waves and High-Temperature Hydrodynamic Phenomena, vols. 1 & 2 (Academic Press, New York, 1966 and 67), Chap. 2
3. G.N. Minerbo, Maximum entropy Edington factors. J. Quant. Spectrosc. Radiat. Transf. **20**, 541–545 (1978)
4. M. Mori, M. Umemura, A. Ferrara, The nature of Lya Blobs: Supernova-dominated primordial galaxies. Astrophys. J. **613**, L97–L100 (2004)
5. T.-G. Lee, M. Busquet, et al., Radiative and atomic properties of C and CH plasmas in the warm-dense-matter regime. Phys. Rev. E **98**, 043203 (2018)
6. H.G. Wei et al., Opacity studies of silicon in radiatively heated plasma. Astrophys. J. **683**, 577–583 (2008)

7. Q.-L. Dong et al., Characteristic measurements of silicon dioxide aerogel plasmas generated in a Planckian radiation environment. Phys. Plasmas **17**, 012701 (2010)
8. D. Salzmann, *Atomic Physics in Hot Plasmas* (Oxford University Press, 1998)., Chap. 7
9. N. Vinyoles et al., A new generation of standard solar models. Astrophys. J. **835**, 202 (16pp) (2017)
10. J.C. Pain, F. Gilleron, M. Comet, Detailed opacity calculations for astrophysical applications. MPDI Atoms **5**, 22 (2017). https://doi.org/10.3390/atoms5020022
11. E.S. Dodd et al., Hohlraum modeling for opacity experiments on the national ignition facility. Phys. Plasmas **25**, 063301 (2018)
12. D.B. Sinars et al., Review of pulsed power-driven high energy density physics research on Z at Sandia. Phys. Plasmas **27**, 070501 (2020)
13. J.E. Bailey et al., A higher-than-predicted measurement of iron opacity at solar interior temperatures. Nature **517**, 56 (2015)
14. T. Nagayama, Systematic study of L-Shell opacity at stellar interior temperatures. Phys. Rev. Letts. **122**, 235001 (2019)
15. R.M. More, S.B. Hansen, T. Nagayama, Opacity from two-photon processes. High Energy Density Phys. **24**, 44 (2017)
16. J.R. Lee et al., A search for pulsations in the optical light curve of the Nova ASASSN-17hx. Astrophys J **869**, 7 (8pp) (2018)
17. A. Heger et al., How massive single stars end their life. Astrophys. J. **591**, 288–300 (2003)
18. M. Kato, I. Hachisu, Optically thick winds in nova outbursts. Astrophys. J. **437**, 802 (1994)
19. H.A. Bethe, J.R. Wilson, Revival of a stalled supernova shock by neutrino heating. Astrophys. J. **295**, 14–23 (1985)
20. S. Richers et al., A detailed comparison of multidimensional Boltzmann Neutrino transport methods in core-collapse supernovae. Astrophys. J. **847**, 133 (21pp) (2017)
21. K. Sumiyoshi, S. Yamada, Neutrino transport in three dimensions for core-collapse supernovae I. Static configurations. Astrophys. J. Suppl. Ser. **199**, 17 (32pp) (2012)
22. W. Iwakami, Simulations of the early post-bounce phase of core-collapse supernovae in three-dimensional space with full Boltzmann Neutrino Transport. Astrophys. J. **903**, 82 (24pp) (2020)
23. H.-T. Janka, Neutrino emission from supernovae. *arXiv preprint arXiv:1702.08713* (2017)
24. S. Yamada, Proceedings of the Japan Academy, Ser. B (2024 in press)